RSC Advances



PAPER

View Article Online
View Journal | View Issue



Cite this: RSC Adv., 2025, 15, 11774

Defect-enriched CuO/CeO₂ nanostructure: indepth structural characterization and photocatalytic performance†

Ajit Kumar Dhanka,^a Balaram Pani D^b and Nityananda Agasti *

The catalytic activity of CeO₂ can be modulated by incorporating defects and inducing strong metalsupport interactions. Herein, we introduce CuO into CeO₂ for generating oxygen vacancies (CeO_{2-x}) via the interaction between CuO and CeO2. The resultant catalyst CuO/CeO2 exhibited improved performance for the photocatalytic degradation of isoproturon (a herbicide). The improvement in catalytic performance was attributed to the oxygen vacancies and interfacial charge transfer between CuO and CeO2. Notably, the addition of CuO increased the oxygen vacancies in CeO2, correlating with the increase in the Ce3+ content (31.2%). X-ray photoelectron spectroscopy (XPS) and Raman spectroscopy studies substantiated the increase in surface oxygen vacancies in CeO₂. We investigated the oxygen vacancies quantitatively and detected the chemical states of the Cu and Ce species. Photoluminescence (PL) studies validated the role of oxygen vacancies in restraining the recombination of photogenerated electron and hole pairs, thereby improving the catalytic activity of CuO/CeO2. Trapping experiments were conducted to identify the reactive species involved in the photocatalytic degradation process. Based on a thorough evaluation of the characteristics of the catalyst and photocatalysis experimental outcomes, a potential reaction mechanism was proposed. Furthermore, high-resolution mass spectrometry (HRMS) analysis was utilized to identify degradation intermediates, enabling us to outline the possible degradation pathways of isoproturon. Isoproturon (IPU) was effectively degraded under UV light with CuO/CeO₂ compared with pristine CeO₂. A 95% degradation efficiency was achieved with CuO/CeO₂ (10 mg) for the IPU solution (10 μ g L⁻¹) within 120 minutes. This study provides detailed insights into the structural analysis of defective CeO2 and an in-depth mechanism of its photocatalysis, facilitating the design of high-performance ceria-based catalysts for photocatalytic degradation of emerging contaminants in water.

Received 27th January 2025 Accepted 28th March 2025

DOI: 10.1039/d5ra00640f

rsc.li/rsc-advances

1 Introduction

Pesticides are a group of chemical substances that include insecticides, rodenticides, molluscicides, fungicides, herbicides, and nematicides. They are used to control pests, such as insects, fungi, weeds, rodents, spiders, ticks, mites, birds, slugs, snails, and nematodes, which can significantly harm crop

production.^{1,2} The annual loss of food due to pests is estimated to be 45%.³ Keeping the demand for food in mind, crop productivity enhancement requires the application of pesticides. Approximately 3 million tons of pesticides are applied each year to agricultural fields globally, which is a value 15 to 20 times higher than those for the last three decades.⁴ Alternatively, the widespread use of pesticides in agriculture raises critical concerns owing to their persistence and potential toxicity to the ecosystem and human health.⁵⁻⁷ Pesticide residues detected in vegetables, fruits, agricultural lands, and even in drinking water cause various diseases.⁸ Pesticide contamination poses a higher risk of developing cancers in organs, including the kidneys, lungs, and stomach.^{9,10}

Commonly applied pesticides in agriculture include isoproturon, glyphosate, acephate, propoxur, metaldehyde, diazinon, chlorpyrifos, dichlorodiphenyltrichloroethane (DDT), and malathion. Among these, "N,N-dimethyl-N'-[4-(1-methylethyl) phenyl]urea" or "3-(4-isopropylphenyl)-1,1-dimethylurea", which is commercially known as isoproturon (IPU) ($C_{12}H_{18}N_2O$), belongs to the phenylurea family, ¹¹ and it is widely

^aDepartment of Chemistry, University of Delhi, North Campus, Delhi 110007, India. E-mail: nnagasti@chemistry.du.ac.in

^bDepartment of Chemistry, Bhaskaracharya College of Applied Sciences, University of Delhi, Dwarka, New Delhi, 110075, India

[†] Electronic supplementary information (ESI) available: UV-vis absorption spectra, UV-vis DRS spectra, FTIR spectra, comparison of powder XRD peak, Raman peak shifting and intensity variation, XPS spectra of CeO₂, calculation of the Ce³⁺ content from Ce 3d XPS spectra, oxygen vacancy calculation from O 1s in XPS spectra, O 1s XPS spectra, thermal stability evaluation, kinetic and isotherm model study, photocatalytic degradation of IPU under UV light irradiation and dark condition monitored using UV-vis spectroscopy, scavengers test, possible degradation pathway, and fragmentation pattern based on HRMS analysis. See DOI: https://doi.org/10.1039/d5ra00640f

used to prevent the growth of unwanted plants or broad-leaved weeds in cotton, wheat, cereal, and sugarcane fields and citrus, and asparagus fruit farms.12 Although the herbicide IPU helps in farming, its toxicity causes adverse effects on the ecosystem.¹³ The Lethal Dose 50 (LD_{50}) toxicity (the dose that results in death of 50% of a test group of animals, usually mice) of isoproturon for rats is 1826 mg kg⁻¹ when ingested orally, and more than 2000 mg kg⁻¹ when it encounters the skin. 14,15 IPU also affects the photosystem II (PSII) in plants by inhibiting electron transport and consequently promoting oxidative stress.16 Due to its poor biodegradation, low volatility, low tendency to sorb to soil and high solubility in water (65 mg L^{-1} at 22 °C), it persists in water. 17,18 In water, the half-life cycle of IPU is 1210, 1560 and 540 days at pH 5, 7 and 9, respectively.19 Reupert et al. have detected the concentration of IPU to be in the range of 0.1 to $0.125 \mu g L^{-1}$ in surface water and 0.05 to $0.1 \mu g L^{-1}$ in groundwater in Germany. Sometimes, the level of IPU in drinking water has been investigated to be more than 0.1 µg L⁻¹. Another study reports that approximately one-third of the surface water is contaminated with IPU in the concentration range of 0.01 to 0.06 μg L⁻¹ in Wielkopolska Province in Poland.21 IPU residues have been found worldwide in different environments at concentrations that often exceed the allowed limit of 0.1 μ g L⁻¹.^{22,23} Isoproturon has been included in the list of the 33 most potential water contaminants.24 It has been reported that IPU can harm the human immune system and disrupt the thyroid gland or thyroid hormones.25,26 It is a deadly

carcinogen for human health. Therefore, it is imperative to

develop a suitable approach for the degradation of IPU in water.

Among various methods,27-34 photocatalytic degradation, owing to low cost, stability and high efficiency, has received much attention for the decomposition of residual pesticides in wastewater.35,36 Additionally, the use of light irradiation for the catalytic decomposition of pollutants offers a sustainable solution to combat water contamination.³⁷ Besides light, the role of the catalyst material is also important for the efficient degradation of contaminants in water. As photocatalysts, metal oxides are effective due to their tunable band gap, which is sensitive to light for producing electron-hole pairs responsible for the chemical conversion of molecules. Among various metal oxides³⁸⁻⁴⁰ CeO₂ has been found to be more effective owing to its excellent redox catalytic property facilitated by the reversible interconversion of Ce4+ and Ce3+.41 Additionally, CeO2, with a band gap of approximately 3.3 eV, can absorb light in the near UV region, and to a lesser extent, in the visible region, making it a promising photocatalyst, especially at the nanoscale.42 The band gap of CeO2 nanoparticles can be modified to regulate its catalytic properties. The flexible interconversion of oxidation states between Ce4+ and Ce3+ generates defects in CeO2, thus modifying its catalytic properties. The most favorable defect is oxygen vacancies, Ce⁴⁺-O_V-Ce³⁺ (O_V - oxygen vacancy), generated in the CeO₂ lattice structure. Thus, the catalytic property of CeO₂ can be regulated by modulating its oxygen vacancies. The addition of metal or metal oxide nanoparticles into CeO2 is an effective strategy to enhance oxygen vacancies due to strong synergistic metal-CeO₂ interactions. This interaction enhances interfacial redox reactions and promotes the formation of oxygen vacancies. 43 Though there are reports on the increase in ${\rm CeO_2}$ defects caused by the addition of metals and metal oxide nanoparticles, $^{44-46}$ there is scope to study defect-induced photocatalytic activity of ceria-based materials. Moreover, studies on the photocatalytic degradation of isoproturon by ceria-based materials and in-depth mechanistic studies along with degradation patterns are limited.

Therefore, considering the effectiveness of the defectmediated catalytic property of CeO2 and the need for efficient photocatalytic degradation of pesticides in water, the present study reports the preparation of CuO/CeO₂ and evaluation of its photocatalytic performance for the degradation of isoproturon. This study provides a detailed insight into the structural characterization of defects in CeO2, including the estimation of oxygen vacancies based on Raman and XPS studies. Herein, we introduce CuO into CeO₂ for generating oxygen vacancies (CeO_{2-x}) and found that CuO/CeO2 showed markedly enhanced photocatalytic activity. Structural characterization confirms the generation of oxygen vacancies and interfacial charge transfer between CuO and CeO2. The photocatalytic efficiency of CuO/CeO2 nanocomposites was evaluated by the degradation of isoproturon (IPU) in an aqueous medium under UV light exposure, representing a model system for pesticide removal from wastewater. The degradation process was monitored using UV-vis absorption spectroscopy. Compared to pristine CeO2, the CuO/CeO2 exhibited superior photocatalytic performance at room temperature. To determine the active species responsible for the degradation, trapping experiments were performed. A detailed investigation into the reaction mechanism was conducted, leading to the proposal of a possible degradation pathway for IPU. The results suggest that the interaction between CuO and CeO2 generates oxygen vacancies, which facilitate the dissociation of water molecules into 'OH radicals and promote the reduction of O₂ to 'O2 species. These reactive species, 'OH and 'O2, significantly enhance the photocatalytic degradation of IPU in water.

2 Experimental section

2.1 Materials

All chemicals utilized were of analytical grade and used directly without further purification. A reported method⁴⁷ was followed to prepare the CuO/CeO_2 nanocomposite. Cerium nitrate hexahydrate (99%) ($\text{Ce(NO}_3)_3 \cdot 6\text{H}_2\text{O}$), sodium hydroxide (98%) (NaOH) and isoproturon ($\text{C}_{12}\text{H}_{18}\text{N}_2\text{O}$) were purchased from CDH India; copper nitrate ($\text{Cu(NO}_3)_2$) was purchased from Merck; ethanol ($\text{C}_2\text{H}_5\text{OH}$), methanol (CH_3OH), ethylenediaminetetraacetic acid (EDTA), p-benzoquinone (pBQ) and tert-butyl alcohol (t-BuOH) were purchased from Sigma-Aldrich India.

2.2 Preparation of CuO/CeO₂

The CuO/CeO₂ nanocomposites were synthesized using cerium nitrate (Ce(NO₃)₃·6H₂O) and copper nitrate (Cu(NO₃)₂) via a solvothermal method, as shown in Scheme 1.⁴⁸ In a typical preparation route for CuO/CeO₂ nanocomposites with a 1:10 wt. ratio, 0.1 g of Cu(NO₃)₂ and 1.0 g of Ce(NO₃)₃·6H₂O were dissolved in



Scheme 1 Preparation of CuO/CeO₂ nanocomposites via the solvothermal method.

50 mL of methanol solution. 0.25 g of sodium hydroxide (NaOH) was added to the solution while stirring vigorously for 30 minutes. The resulting mixture was transferred to a Teflon-lined stainless-steel autoclave and heated at 180 °C for a duration of 18 hours in an oven. The autoclave was allowed to cool gradually to room temperature. The solid precipitate formed was collected and subsequently washed with ethanol through centrifugation at 3000 rpm for 10 minutes, and the washing was repeated 3-4 times. Finally, the precipitate was dried at 80 °C for 4 hours and calcined at 250 °C for 2 hours to obtain the CuO/CeO₂ nanocomposites. For comparison, CeO2 nanoparticles were prepared using the same method, except for the addition of Cu(NO₃)₂. CuO nanoparticles were synthesized using a method similar to that of CeO₂ nanoparticles, with the only modification being the precursor. All the remaining steps of the synthesis followed the same procedure as used for CeO2 nanoparticles.

2.3 Sample characterizations

The structural and morphological features of the synthesized nanocomposites were analyzed using multiple characterization techniques. The powder X-ray diffraction (PXRD) for CuO/CeO₂, CeO₂ and CuO was performed. The X-ray diffraction (XRD) patterns were recorded using a Rigaku Miniflex X-ray diffractometer equipped with a Cu K α anode ($\lambda = 0.1542$ nm) operated at 40 kV and 15 mA. Data were collected in the 2θ range from 20° to 80°, with a step size of 0.02° per step and a scan rate of 3° per minute. The obtained diffraction patterns were matched with the reference pattern of the JCPDS database. The FTIR spectra of the samples were recorded using a Nicolet™ iS50 Fouriertransform infrared (FTIR) spectrometer in the wavelength range of 500-4000 cm⁻¹ with KBr pellets at a resolution of 4 cm⁻¹ and in the attenuated total reflection (ATR) mode. To understand the optical behavior of the materials, the UV-visible spectra of the powder sample dispersed in water were obtained by a Shimadzu UV-1800 spectrophotometer (Shimadzu, Japan). The sample was first placed on the sample holder, and its absorbance was measured in the wavelength range of 200 to 800 nm with deuterium and tungsten-halogen lamps as light sources. The UV-vis diffuse reflectance spectroscopic (DRS) measurements were carried out using an Agilent Cary 5000 in the wavelength range from 200 nm to 800 nm at a resolution of 1 nm, and the samples were used in the powder form. The Raman spectroscopic analysis was performed using an Invia

Reflex Renishaw microscope with a 532 nm, 50 mW diode laser in the wave number range from 100 cm⁻¹ to 900 cm¹, and the samples analyzed were in powder form. A field emission scanning electron microscope (FESEM) with Oxford-EDX system IE 250 X Max 80 (FEI Quanta 200 F SEM) was used to study the morphology of CuO/CeO2 and CeO2. The elemental composition of the samples was analyzed using energy-dispersive X-ray spectroscopy (EDX). Moreover, to gain a thorough insight into the packing pattern of CuO/CeO2 nanocomposites, highresolution transmission electron microscopy (HRTEM) images were collected using a transmission electron microscope TEC-NAI G20 HR-TEM 200 kV. Thermogravimetric analysis (TGA) was also performed on HITACHI STA7300 up to 600 °C in a nitrogen atmosphere with a controlled gas flow of 150 bar. The samples were analyzed in the alumina crucible at a heating rate of 10 °C min⁻¹ to determine their thermal stability. The surface area and pore size of the synthesized materials were evaluated using an Autosorb-iQ XR analyzer (Quantachrome Instruments) through N2 adsorption/desorption isotherms. Before the analysis, the samples underwent degassing under vacuum (\sim 1 \times 10⁻⁵ bar) at 150 °C for 10 hours. The adsorption/desorption isotherm measurements were then conducted in a liquid nitrogen bath at 77 K. X-ray photoelectron spectroscopy (XPS), using a Kratos Axis Supra Plus XPS equipped with a monochromatic Al Ka X-ray source (1486.6 eV), was employed to study the surface elemental oxidation state and composition of samples. The high-resolution mass spectrometric (HRMS) technique G6530AA (LC-HRMS-Q-TOF) with the ESI and APCI source was used to identify the possible degradation intermediates and pathways. The photoluminescence (PL) study was performed at room temperature on Horiba Yvon PTI Quanta-Master (8450-11) spectrophotometer using an excitation source of 375 nm nano-LED. The charge carrier lifetimes are ascerusing time-resolved photoluminescence (TRPL) measurements (in micro and milliseconds) employing a 980 nm laser and xenon lamp as the source in modulated mode.

2.4 Photocatalytic degradation of isoproturon under UV light irradiation

To investigate the photocatalytic degradation of isoproturon (IPU), the as-synthesized CuO/CeO $_2$ nanocomposites (10 mg) were dispersed in a 100 mL aqueous solution of IPU (10 $\mu g \, L^{-1}$) and the content was kept under a custom-built solar reactor,

illuminated by a 125 W high-pressure mercury lamp (Hg) (Osram, India) emitting UV light (λ < 400 nm), for 2 hours with stirring at room temperature. At every 20 minutes interval, 5 mL aliquots of the suspension were withdrawn and transferred into vials, then centrifuged at 8500 rpm for 10 minutes to precipitate the catalyst particles. Following a typical procedure, 49 the supernatant was carefully collected and transferred into a quartz cuvette to measure the UV-vis absorption spectra. The IPU solution, along with the catalyst particles, was reintroduced into the reaction vessel after the absorbance measurement. At specific time intervals, the absorbance was measured to monitor the decomposition rates of isoproturon. To assess its reusability, the catalyst was separated from the reaction mixture via centrifugation after the reaction, washed with deionized water and then dried at 80 °C for three hours. The dried catalyst was then reintroduced into a fresh isoproturon solution, and the photocatalytic procedure was repeated to evaluate its efficiency. Additionally, control experiments were conducted using CuO and CeO2 individually under identical conditions to compare their photocatalytic performances.

To assess the photocatalytic performance of the CuO/CeO₂ catalyst, the UV-vis absorption spectra were recorded in the range of 200-325 nm both in the presence and absence of the catalyst under UV light irradiation and in the dark. Blank experiments were performed with an aqueous solution of IPU (i) under the dark condition (without UV light irradiation) (see Fig. S9d-g ESI†) and (ii) in the presence of UV light irradiation (see Fig. S9a-c ESI†). The blank experiment in the absence of UV light irradiation shows negligible degradation of IPU, suggesting the important role of UV light irradiation. Further, the negligible degradation of IPU in the presence of UV light irradiation shows the need for a catalyst. Further, to investigate the role of CuO in the degradation of isoproturon, experiments were conducted with CuO/CeO2, CuO and pristine CeO2 catalysts under UV light irradiation at identical experimental conditions.

2.5 Free radical and hole scavenging experiments

To investigate the mechanism and the principal active species responsible for the photocatalytic degradation of IPU in water under UV light irradiation using CuO/CeO2 as a catalyst, experiments were conducted with the addition of scavengers. The scavengers quench the reaction between the reactive species and the IPU molecule. To understand the role of scavengers, the photocatalytic experiments were performed with and without scavengers under identical reaction conditions. Here, tert-butyl alcohol (t-BuOH) was added to the reaction system as a scavenger for 'OH, EDTA for photogenerated holes (h⁺), AgNO₃ for photogenerated electrons (e⁻) and p-benzoquinone (pBQ) for superoxide anion radicals (${}^{\cdot}O_2^{-}$). The effects of various scavengers on the photocatalytic degradation of isoproturon are illustrated in Fig. 5f and S10 ESI.† Based on the result, photocatalytic degradation in the presence of scavengers follows the order EDTA (56%) < AgNO₃ (61%) < t-BuOH (87%) < pBO (91%) < no scavenger (95%). The results showed that the addition of EDTA and AgNO3 significantly inhibited the degradation of isoproturon, suggesting that h⁺ and e⁻ are the active

species playing an important role in the photocatalytic degradation of isoproturon.

3 Result and discussion

Structure, morphology and elemental analysis

The optical properties were studied to understand the formation of CuO/CeO2 nanocomposites using UV-vis spectroscopy. The band at 303 nm corresponds to CeO₂ nanoparticles; however, in the spectra of CuO/CeO2 nanocomposites, the bands at 268 and 299 nm correspond to CuO and CeO₂, respectively^{49,50} (Fig. 1a). The band at 268 nm corresponding to the surface plasmon absorption of CuO suggests the existence of CuO in the CuO/ CeO₂ nanocomposites.⁵¹ The band at 299 nm is due to CeO₂, which suffers a blue shift compared to pristine CeO2 nanoparticles⁵² (Fig. S1 ESI†). This can be attributed to the decrease in the band gap in CuO/CeO2 53 on account of the fact that incorporating CuO onto CeO2 introduces impurity energy levels between the valence and conduction bands, consequently narrowing the band gap in CuO/CeO2. The reduction in band gap was also verified from the UV-vis diffuse reflectance spectra (DRS) (Fig. S2 ESI†) using the Kubelka-Munk (K-M) function. The plot of the Kubelka-Munk (K-M) function,

$$\alpha h \nu = A(h \nu - E_s)^{n/2} \tag{1}$$

against the energy of the light gives the band gap energy (E_g) , where α , A, h, ν , $E_{\rm g}$ correspond to the absorption coefficient, a constant, Planck's constant, light frequency, and band gap energy, respectively.54 The band gap energy was estimated to be 3.2 eV for CuO/CeO₂ and 3.3 eV for CeO₂ (Fig. 1b).

The optical properties suggest the incorporation of CuO on the surface of CeO₂. Furthermore, the bands in the FTIR spectra of CuO/CeO₂ nanocomposites at 698 cm⁻¹ and 745 cm⁻¹, corresponding to Ce-O and Cu-O, respectively, suggest the formation of the composites (Fig. S3 ESI†).55 The formation of the composites is also inferred by assessing the thermal stability of CuO/CeO2. Thermogravimetric analysis (TGA) was performed for both the CuO/CeO2 nanocomposite and pure CeO₂ nanoparticles (Fig. S8 ESI†). CuO/CeO₂ exhibited higher thermal stability than pristine CeO2, suggesting the formation of the composite material.

To understand the structural characteristics of CuO, CeO₂ and CuO/CeO₂ nanocomposites, powder X-ray diffraction (XRD) analysis was carried out. In the PXRD patterns of CuO presented in Fig. S4b ESI,† the prominent diffraction peaks observed at 2θ 29.2°, 31.5°, 35.5°, 38.7°, 42.4°, 45.4°, 48.4°, 55.5°, 58.2°, 61.5°, 66.2°, 68.2°,72.3° and 75.3° correspond to the (115), (303), (-111), (111), (200), (200), (-202), (426), (020), (202), (-113), (-310), (311) and (282) crystallographic planes matching with the monoclinic structure of CuO, and two planes at 45.4° and 72.3° correspond to the (200) and (311) planes matching the Cu₂O.⁵⁶ These peaks confirm the formation of the CuO nanoparticle structure, which is consistent with JCPDS card no. 01-1117.⁵⁷ In the XRD pattern (Fig. 1c), the peaks at 2θ ; 28.4°, 32.9°, 47.5°, 56.3°, 59.0°, 69.3°, 76.7°, and 78.8° correspond to the (111), (200), (220), (311), (222), (400), (331), and (420)

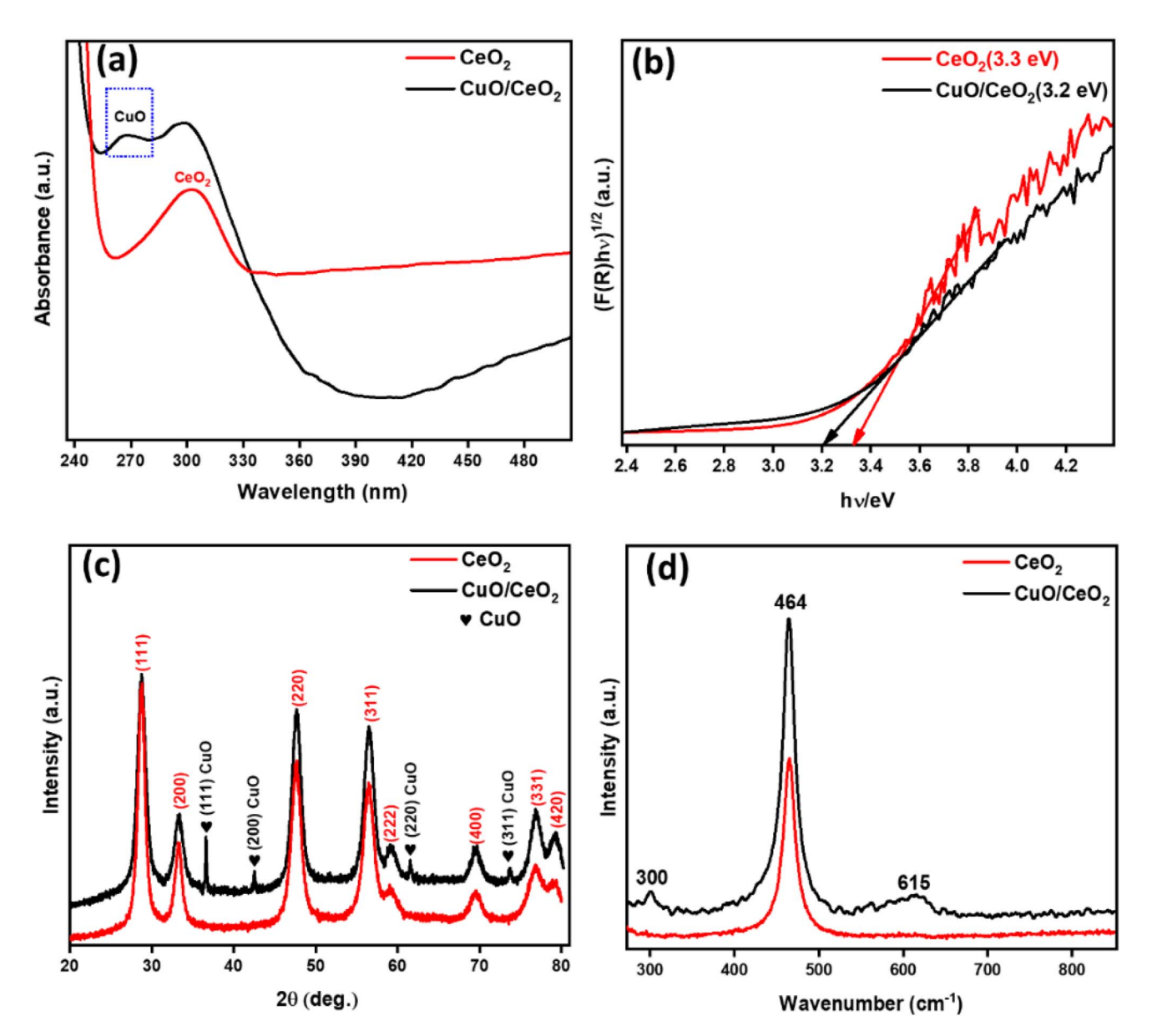


Fig. 1 Characterization results of CeO_2 and CuO/CeO_2 nanocomposites: (a) UV-vis absorption spectra, (b) band gap energy estimation using UV-vis diffuse reflectance spectroscopy (DRS) and the Kubelka–Munk (K–M) function, (c) powder X-ray diffraction (PXRD) patterns, revealing the crystalline structure and phase composition. (d) Raman spectra, providing insights into the vibrational properties and defect states of the materials.

crystallographic planes, respectively. The XRD pattern of pristine CeO_2 nanoparticles matches with the cubic fluorite structure of CeO_2 (JCPDS file number 34-0394).⁴⁹ Besides, the peaks corresponding to CuO appear at 2θ ; 36.7° , 42.5° , 61.5° and 73.5° (JCPDS file no. 78-0428),⁵⁸ suggesting the formation of CuO/CeO₂ composites. The diffraction peaks of CuO/CeO₂ shift to lower 2θ angles compared to pristine CeO_2 , with the most prominent shift occurring in the highly intense peak of CuO/CeO₂ associated with the (111) diffraction plane at a 2θ of 28.7° (Fig. S4a ESI†). This shift in diffraction peaks suggests the anchoring of CuO on the CeO_2 surface. Additionally, there is a decrease in intensity and broadening of the peaks, indicating

a reduction in crystallite size. The crystalline size can be estimated using the Scherrer equation, ⁵⁹

$$D = K\lambda/\beta\cos\theta\tag{2}$$

where D is the average crystallite size (nm), K is a dimensionless shape factor typically set to 0.98 for spherical crystals, $\lambda=1.54$ Å, θ is the Bragg angle (half of the 2θ angle where the peak occurs), corresponding to the most intense or primary diffraction peak of CeO₂, observed at 2θ 28.4° and β is the full-width at half-maximum (FWHM) of the primary diffraction peak. The average crystallite size was determined to be 6.6 nm for CeO₂ in CuO/CeO₂ nanocomposites and 7.7 nm for pristine CeO₂. Moreover, the

decrease in the intensity of diffraction peaks can be ascribed to the formation of defects on the surface of ceria. Khan *et al.* reported that the shift in diffraction peaks towards a lower angle corresponds to an increase in oxygen vacancies in CeO₂.⁶⁰ In the present case, the shifting of diffraction peaks to lower angles suggests an increase in oxygen vacancies in CuO/CeO₂.

To evaluate the formation of defects in CuO/CeO2 nanocomposites, the Raman spectra of pristine CeO₂ and CuO/CeO₂ nanocomposites were recorded in the range of 280-850 cm⁻¹ (Fig. 1d). In the spectra, a prominent and intense peak at 465 cm⁻¹ corresponds to the F_{2g} symmetric stretching mode of the Ce-O bond, a characteristic of the fluorite crystal structure of CeO₂.61 The F₂₀ peak for CuO/CeO₂ appears at 464 cm⁻¹, with a downshift compared to the pristine CeO₂ (Fig. S5a ESI†). Additionally, a band appearing at 300 cm⁻¹ corresponds to the tenorite phase of copper oxide (CuO), which confirms the presence of Cu in the form of CuO.62 The downshift in the F_{2g} peak for CuO/CeO2 can be ascribed to the formation of oxygen vacancies due to the introduction of CuO63,64 (Fig. S5a ESI†). Besides, there is a band at 615 cm⁻¹, which is also accounted for the defect-induced (D) mode representing oxygen vacancies. 65,66 The absence of this band in pristine CeO₂ confirms the role of the interfacial interaction between CuO and CeO2, providing information on the oxygen vacancies in CuO/CeO2. Moreover, oxygen vacancies can also be related to the FWHM of the F_{2g} peak. An increase in the FWHM of the F2g peak indicates an increase in the oxygen vacancies in CuO/CeO2,67 which are quantified from the crystallite size of CeO₂. The crystallite size of CeO2 is calculated from the F2g peak using the relation

$$\Gamma \text{ (cm}^{-1}) = 5 + 51.8/d \text{ (nm)}$$
 (3)

where Γ is the half-width at half maximum (HWHM). The crystallite size, d in nm,^{68,69} was determined to be 11.51 nm for pristine CeO₂ and 12.95 nm for CuO/CeO₂, which are consistent with the values obtained from XRD and HRTEM analyses. The d values obtained from Raman spectra were used to calculate the concentration of oxygen vacancies using the following formula:

$$L \text{ (nm)} = \sqrt[3]{\left(\frac{r}{2d}\right)^2 \left[(d-2r)^3 + 4d^2r \right]}$$
 (4)

$$N = 3/4\pi L^3 \tag{5}$$

L represents the correlation length (*i.e.*, the average distance between two lattice defects), r is the radius of the CeO $_2$ units (0.31 nm) and N is the oxygen vacancy concentration in cm $^{-3}$. The concentration of oxygen vacancies was determined to be $8.43 \times 10^{20} \ {\rm cm}^{-3}$ for CuO/CeO $_2$, which is higher than that of pristine CeO $_2$ (7.45 \times 10 $^{20} \ {\rm cm}^{-3}$). Moreover, the ratio of the integrated area of the D peak to the F $_{2g}$ peak (denoted as $I_{\rm D}/I_{\rm F}_{2g}$ reflects the relative concentration of oxygen vacancies on the surface of CuO/CeO $_2$ and CeO $_2$. Compared to pristine CeO $_2$, the $I_{\rm D}/I_{\rm F}_{2g}$ ratio for the CuO/CeO $_2$ nanocomposite exhibits a significant increase. This increase can be attributed to the strong interactions between the CuO and CeO $_2$. As shown in Fig. S5b (ESI †), the $I_{\rm D}/I_{\rm F}_{2g}$ ratio is higher in CuO/CeO $_2$ (0.123) than in

 CeO_2 (0.006). The presence of CuO in CuO/CeO₂ can also be supported by the increase in intensity of the F_{2g} peak due to the strong optical absorption associated with the surface-enhanced Raman scattering effect (SERS).^{71,72}

Photoluminescence (PL) spectroscopy is a sensitive technique used to analyze the defects, oxygen vacancies and effectiveness of trapping charge carriers in semiconductor materials. Therefore, photoluminescence was used to investigate the role of oxygen vacancies in separating photogenerated electron-hole pairs in the CuO/CeO₂ nanocomposites. PL spectra (Fig. 2a) show the UV emission band at 394 nm, which is attributed to the electronic transition from the O_{2p} to Ce_{4f} in CeO₂.73 The decrease in emission observed for CuO/CeO₂ nanocomposites compared to pristine CeO2 suggests that the anchoring of CuO could guench the fluorescence from the CeO₂ nanoparticles. The quenching in emission also indicates the effective separation of charge carriers, resulting from the suppression of their recombination. A lower PL intensity is attributed to a low rate of electron-hole recombination process, consequently increasing the lifetime of photogenerated charge carriers, a favorable factor for the enhancement of photocatalytic performance. Thus, the quenching in PL intensity suggests that the oxygen vacancies on the surface, as well as at the interface of CuO and CeO₂, act as sites to trap the charge carriers, leading to suppression in their recombination, which enhances the photocatalytic performance of the CuO/CeO₂ nanocomposites.⁷⁴

The presence of surface oxygen vacancies in CeO₂ and the oxidation states of Ce and Cu were confirmed by the XPS of CuO/CeO₂. A comparison of the XPS spectra of pristine CeO₂ and that of CuO/CeO₂ evaluated the impact of the CuO incorporation on CeO₂. The XPS survey spectra (Fig. 2b) confirm the elemental composition of the material, showing the presence of Ce, O, and Cu. The characteristic binding energy peaks were observed in the regions: 877–920 eV, 527–535 eV and 925–960 eV for Ce 3d, O 1s and Cu 2p, respectively. The high-resolution data were charge corrected to the reference C 1s signal at 284.4 eV. To understand the oxidation states of Ce, the high-resolution scans in the binding energy range of 877–920 eV were deconvoluted and fitted.

The XPS spectra for Ce 3d can be deconvoluted into eight distinct peaks at the following binding energies (eV): 882.3, 885.2, 888.1, 898.3, 900.9, 903.3, 905.7, and 916.6, as shown in Fig. 2c. Among them, the peaks appearing at 882.3 eV and 900.9 eV are due to Ce^{3+} 3d_{5/2} and Ce^{3+} 3d_{3/2}, respectively, whereas the peaks at 898.3 eV and 916.6 eV correspond to Ce^{4+} 3d_{3/2} and Ce^{4+} 3d_{3/2}, respectively.

This confirms that both Ce³⁺ and Ce⁴⁺ coexist in CeO₂. The existence of Ce³⁺ and Ce⁴⁺ states reveals the presence of O-vacancies in the CeO₂ crystals because of their interconversion from the Ce³⁺ and Ce⁴⁺ states.^{77,78} Compared to pristine CeO₂, the intensity of the Ce⁴⁺ peaks is reduced and that of Ce³⁺ is increased in CuO/CeO₂ (Fig. S6 ESI†). This suggests an increase in the amount of Ce³⁺ due to the addition of CuO into CeO₂, and consequently, more oxygen vacancies are generated in CuO/CeO₂. The Ce³⁺ content can be calculated as the ratio of the sum of the integrated areas of all peaks corresponding to Ce³⁺ to the total area of all the peaks corresponding to Ce 3d in

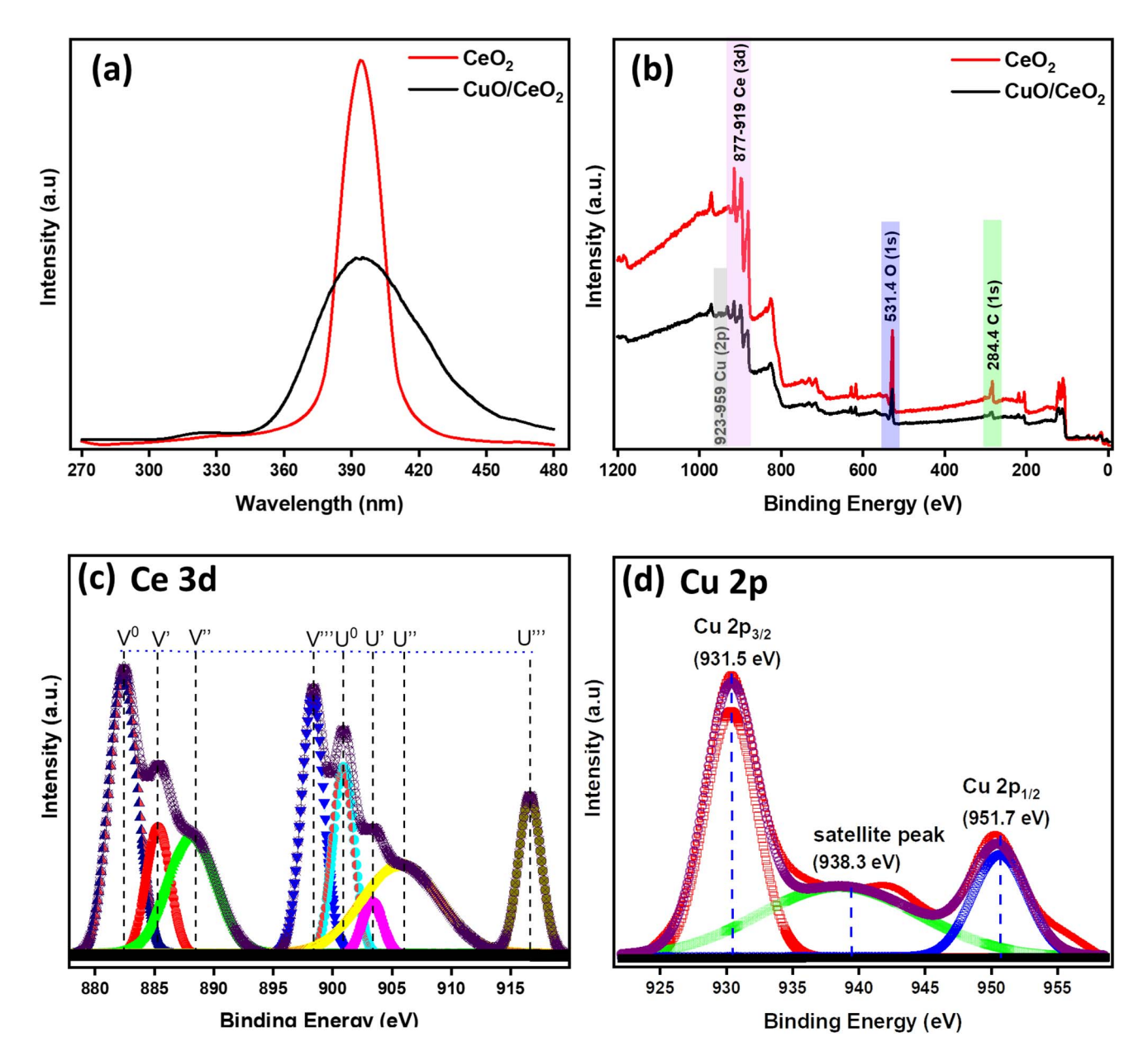


Fig. 2 (a) Photoluminescence spectra of CeO₂ and CuO/CeO₂ nanocomposites. XPS survey spectra of (b) CeO₂ and CuO/CeO₂ and deconvoluted spectra of (c) Ce 3d and (d) Cu 2p.

the XPS spectra (Table S1 ESI†).⁷⁹ In CuO/CeO₂, the atom concentration of surface Ce^{3^+} is estimated to be 31.2%, which is higher than that of pristine CeO_2 (24.2%). Higher Ce^{3^+} corresponds to an increase in oxygen vacancies in CuO/CeO_2 . The presence of CuO can also be confirmed from the Cu 2p spectrum shown in Fig. 2d. The two peaks located at the binding energies of 931.5 eV and 951.7 eV could be ascribed to $(Cu\ 2p_{3/2})$ and $(Cu\ 2p_{1/2})$, respectively. The satellite peak appearing at 938.3 eV is a typical characteristic of Cu^{2^+} species. Further, in the high-resolution XPS spectra of O 1s, distinct peaks were observed at 528.4 eV, 530.1 eV, and 532.7 eV, corresponding to different oxygen species. The peak at 528.4 eV (O_L) is associated with lattice oxygen $(Ce^{4^+}-O^{2^-})$, while the peak at 530.1 eV (O_V) is indicative of oxygen vacancies $(Ce^{3^+}-O^{2^-})$. Additionally, the peak at 532.7 eV (O_C) corresponds to chemisorbed surface

oxygen and hydroxyl groups (-OH).⁸⁰ The peak at 530.1 eV is attributed to the oxygen vacancies.⁶¹

Additionally, oxygen vacancies in CuO/CeO $_2$ and pristine CeO $_2$ can also be assessed by calculating the O_V/O_L ratio $_1^{81}$ derived from the areas under the peaks in the O 1s spectra (Fig. S7 and Table S2 ESI $_1^{\dagger}$). The analysis shows that CuO/CeO $_2$ exhibits a higher O_V/O_L ratio, indicating higher oxygen vacancies compared to pristine CeO $_2$. This is also supported by the greater intensity of the O_V peak in CuO/CeO $_2$ (Fig. S7 ESI $_1^{\dagger}$) relative to pristine CeO $_2$. The results agree with the previous studies.

3.2 Morphological and elemental analysis

The morphology of the synthesized CuO/CeO₂ nanocomposites was investigated using FESEM. Fig. 3a represents the FESEM

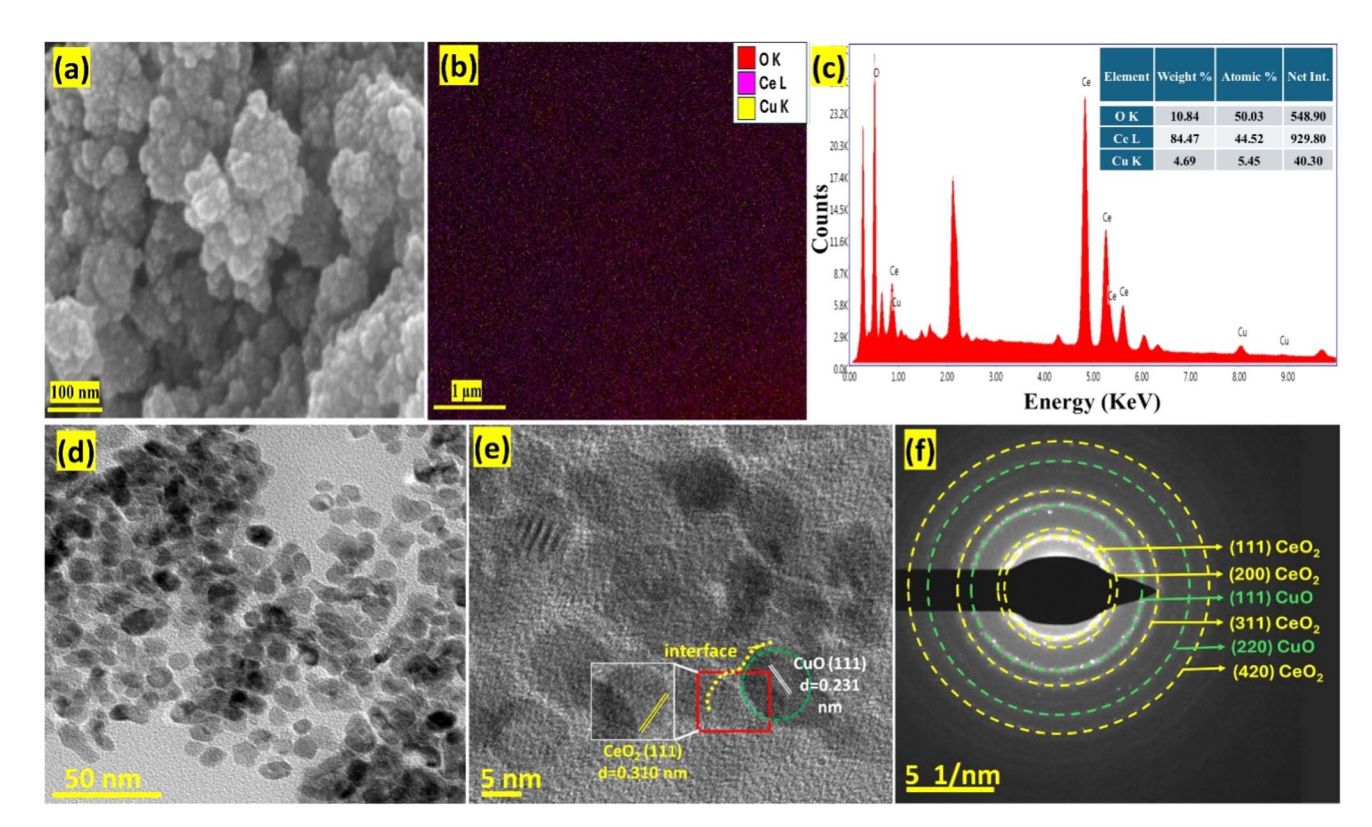


Fig. 3 (a) FESEM images of the CuO/CeO_2 nanocomposites, (b) overlay of Ce + O + Cu and (c) EDX spectra and the corresponding chemical composition analysis, (d) low-resolution TEM image, (e) HRTEM images with lattice fringes and (f) selected area electron diffraction (SAED) sequence of CuO/CeO_2 nanocomposites.

images of CuO/CeO₂ nanocomposites, revealing spherical morphology. The EDX elemental mapping shown in Fig. 3b demonstrates a uniform distribution of cerium (Ce), copper (Cu), and oxygen (O), confirming the successful synthesis of the CuO/CeO₂ nanocomposites. The EDX spectra with atomic and weight percentages of the elements indicate the presence of 84.47% Ce, 4.69% Cu, and 10.84% O, as shown in Fig. 3c.

To ascertain the microstructure of CuO/CeO2 nanocomposites, high-resolution transmission electron microscopy (HRTEM) was conducted (Fig. 3d). The HRTEM image confirms the presence of CuO and CeO2 in the CuO/CeO2 nanocomposites. The lattice fringes of 0.231 nm and 0.310 nm, corresponding to the (111) planes of CuO and CeO₂, respectively (Fig. 3e), clearly identify the presence of CuO and CeO₂. The distinct circles made up of bright spots in the selected area electron diffraction (SAED) pattern (Fig. 3f) of CuO/CeO2 indicate the polycrystallinity of CuO/CeO2 nanocomposites. The interplanar spacings (d values) from a large to a small ring in the SAED pattern for CuO/CeO2 nanocomposites are 0.326, 0.280, 0.195, 0.167, 0.126, and 0.114 nm, which correspond to the crystal planes (111), (200), (111), (311), (220), and (420), respectively. These values closely match with the X-ray diffraction (XRD) pattern of the CuO/CeO₂ nanocomposites. The HRTEM images show the CuO nanoparticles of size 4-7 nm deposited on the surface of CeO₂ nanoparticles, with a size of 6-9 nm, which agrees with the crystallite size calculated from XRD. The HRTEM image (Fig. 3e) of the CuO/CeO₂ nanocomposites reveals that CuO nanoparticles are in close contact with CeO_2 . The interaction between CuO and CeO_2 increases the oxygen vacancies owing to interfacial charge transfer, which plays an important role in improving the photocatalytic performance of CuO/CeO_2 .

To assess the surface area of the CuO/CeO $_2$ nanocomposite, N $_2$ adsorption–desorption isotherm measurement was conducted (Fig. 4). The Brunauer–Emmett–Teller (BET) specific surface area of CuO/CeO $_2$ was found to be 59.85 m 2 g $^{-1}$, which is higher than that of pristine CeO $_2$ (36.01 m 2 g $^{-1}$). The total pore volume and the average pore diameter of CuO/CeO $_2$ were 0.210 cm 3 g $^{-1}$ and 5.40 nm, respectively, whereas those of pristine CeO $_2$ were 0.153 cm 3 g $^{-1}$ and 7.56 nm, respectively. The change in surface properties accounts for the dispersion of CuO on CeO $_2$. The increased surface area of CuO/CeO $_2$ nanocomposites is favorable for more dispersion and high photocatalytic degradation of IPU.

3.3 Catalytic degradation of isoproturon

Isoproturon (IPU) is primarily effective against gramineous (grass-like) weeds. It is typically applied to the soil and can be absorbed by plants, mainly through their roots. Once absorbed, it inhibits weed growth by interfering with the photosynthesis process in plants. Isoproturon exhibits absorption bands at 203 nm and 240 nm, with a lower absorbance shoulder at 275 nm, in the UV-visible spectra^{84,85} (Fig. 5a). Therefore, the degradation of isoproturon can be monitored through its UV-vis absorption spectra.

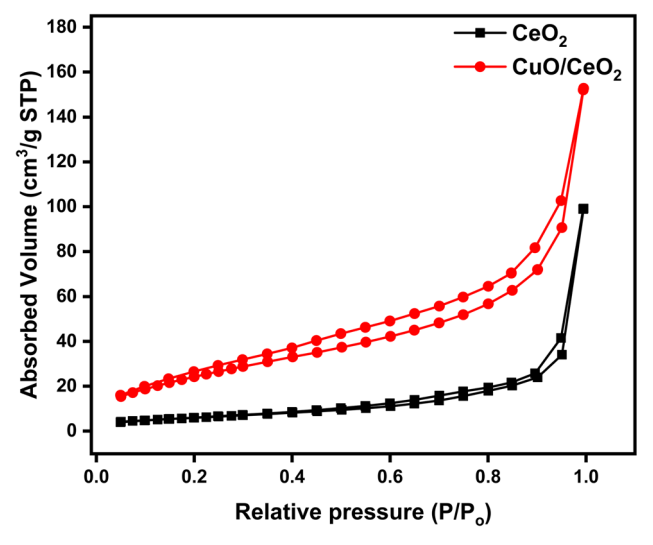


Fig. 4 N_2 adsorption–desorption isotherms of CeO₂ and CuO/CeO₂ nanocomposites.

A 100 mL aqueous solution of IPU (at a concentration of $10 \,\mathrm{mg}\,\mathrm{L}^{-1}$) was treated with 10 mg of the catalyst and exposed to UV light. The progress of the degradation was monitored by the changes in the UV-visible absorption intensities of bands at the wavelengths of 240 and 275 nm with time. With CuO/CeO₂, there was a significant decrease in the intensity and complete disappearance of the bands at 240 and 275 nm within an interval of 120 minutes of UV light irradiation, indicating the

complete degradation of isoproturon (Fig. 5b). However, with CeO_2 and CuO, the band does not disappear completely even after 120 minutes (Fig. S9b and c ESI†). According to the C/C_0 plot, the degradation efficiency of CuO/CeO_2 was approximately 95% (Fig. 5c). The degradation efficiency was calculated using the formula;

Degradation (%) =
$$(C_0 - C_t)/C_0 \times 100\%$$
 (6)

Here, C_0 is the initial concentration, and C_t is the concentration of isoproturon at time t.⁸⁶

To quantitatively assess the degradation efficiency of CuO/CeO₂, the reaction rate constants for the photocatalytic degradation of isoproturon were calculated using the Langmuir–Hinshelwood kinetic model. The degradation of isoproturon in aqueous media follows the pseudo-first-order reaction kinetics, which can be mathematically represented as:

$$-\ln(C/C_0) = kt \tag{7}$$

where C is its concentration at a given time t, C_0 represents the initial concentration of the IPU, and k denotes the first-order rate constant. The linear relationship between $\ln(C/C_0)$ and t is illustrated in Fig. 5d, where the slope of the plot corresponds to the value of k. The calculated rate constants for pristine CeO_2 and CuO/CeO_2 nanocomposites were determined to be $0.01002 \, \mathrm{min}^{-1}$ and $0.01033 \, \mathrm{min}^{-1}$, respectively, indicating an enhancement in photocatalytic performance due to the incorporation of CuO.

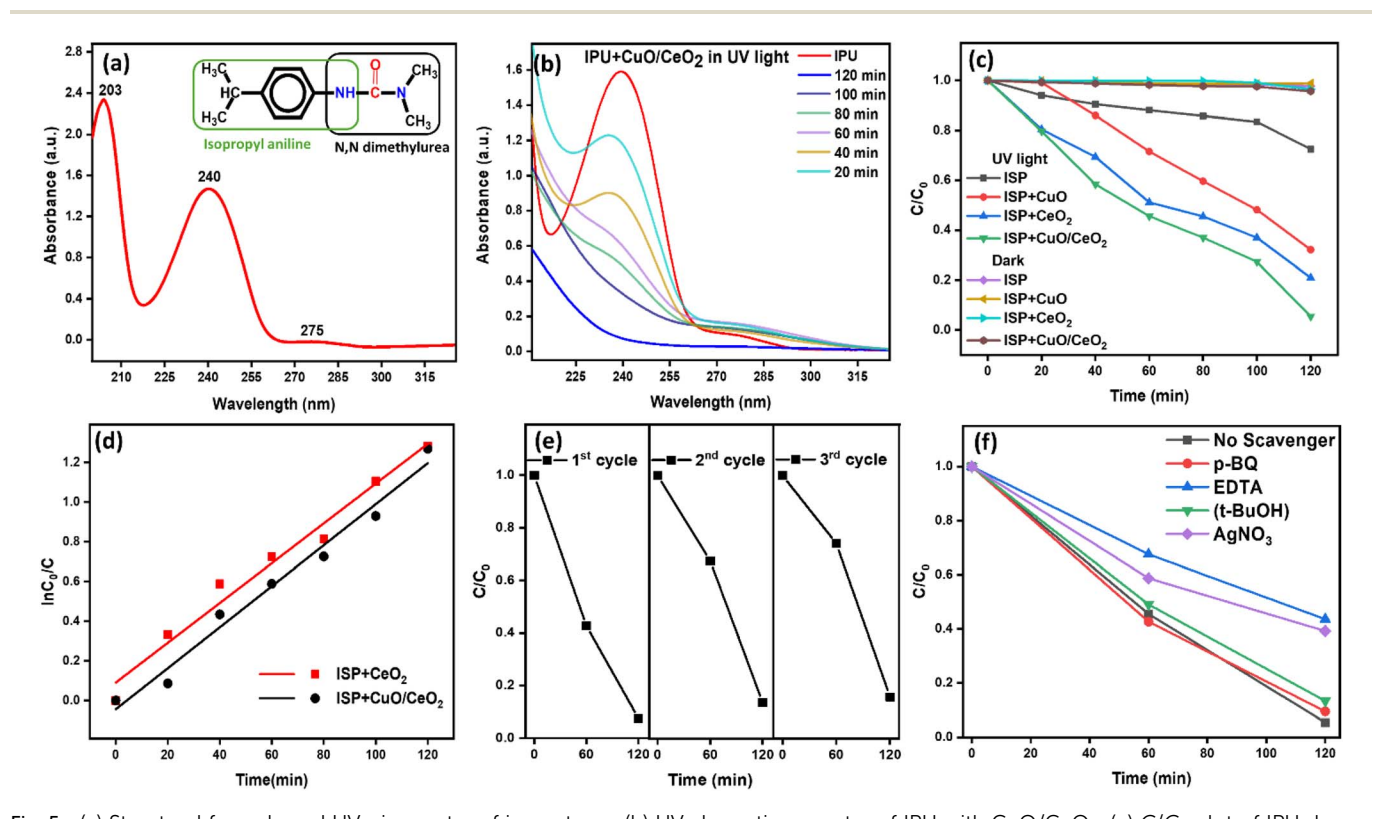


Fig. 5 (a) Structural formula and UV-vis spectra of isoproturon (b) UV absorption spectra of IPU with CuO/CeO_2 , (c) C/C_0 plot of IPU degradation, (d) kinetics of IPU degradation, (e) cyclic runs of the CuO/CeO_2 nanocomposites and (f) photocatalytic activities of CuO/CeO_2 with different scavengers for the degradation of IPU under UV light irradiation.

Table 1 Comparison of the R-square (R^2) values for linear regression using kinetic models for IPU degradation using CeO $_2$ and CuO/CeO $_2$ nanocomposites

	Catalyst	
Key parameters	CeO ₂	CuO/CeO ₂
$q_{\mathrm{e,exp}} \ (\mathrm{mg} \ \mathrm{g}^{-1})$ Pseudo-first-order (PFO) (R^2) Pseudo-second-order (PSO) (R^2)	$q_{ m e} = 9.4571$ 0.99131 0.81424	$q_{\rm e} = 7.9054$ 0.99698 0.79578

3.4 Kinetics study

The adsorption kinetics of isoproturon on the CeO2 and CuO/ CeO₂ nanocomposites were evaluated using two kinetic models: pseudo-first-order (PFO) and pseudo-second-order (PSO)87 (Fig. S11, ESI†). The mathematical equations governing these models are provided in the ESI (eqn (1) and (2)†). The study was conducted at an initial isoproturon concentration of 10 mg L⁻¹ with 10 mg of the catalyst to investigate adsorption behavior over time. To identify the best-fitting kinetic model, key parameters, such as the linear regression correlation coefficient (R^2) and the comparison between the experimental and calculated adsorption capacities (q_e) , were analyzed.⁸⁸ A comparative assessment of R^2 values was performed to determine the most appropriate model, and the corresponding kinetic parameters for each model are summarized in Table 1. The fitting analysis indicates that the photocatalytic degradation of the IPU solution using CeO2 and CuO/CeO2 follows a pseudo-first-order kinetic model, as evidenced by a high R^2 value.

4 Photocatalytic mechanism of IPU degradation

Considering the structural characteristics of CuO/CeO₂ and results obtained from photocatalytic experiments, a possible mechanism is proposed for the photocatalytic degradation of IPU in water catalyzed by CuO/CeO₂ under UV light irradiation and is

shown in Fig. 6. On irradiation of ultraviolet light on the catalyst surface, electrons in the valence band (VB) of CeO₂ absorb energy, become excited and transition to the conduction band (CB), leaving behind holes (h⁺) in the valence band. These h⁺ species act as strong oxidants and interact with the surface adsorbed H₂O, leading to the formation of hydroxyl radicals ('OH). Meanwhile, the excited electrons in the CB of CeO2 are transferred to CuO, which facilitates electron capture and promotes their interaction with the O2 molecules (either dissolved in water or adsorbed on the CuO surface), generating superoxide anion radicals ('O₂-). The presence of CuO enhances the electron transfer rate from the CB of CeO₂ to O₂, thereby improving charge separation.89 Additionally, the photogenerated electrons migrated to CB can be trapped by oxygen vacancies formed by the interfacial interaction between CeO2 and CuO, restraining the recombination of photogenerated charge carriers. This efficient charge separation significantly boosts the photocatalytic activity of CuO/CeO₂.90 The reactive species, 'OH and 'O₂, act as strong oxidants to degrade isoproturon into smaller, non-toxic molecules, which are eventually mineralized into CO2 and H2O.

Formation of exciton (electron and hole, pair)

$$CuO/CeO_2 + h\nu \rightarrow h^+(VB) + e^-(CB)$$

Formation of hydroxyl radicals

$$H_2O + h^+ \rightarrow OH^{\bullet} + H^+$$

$$OH_- + h_+ \rightarrow OH_-$$

Formation of superoxide radicals

$$O_2 + e^- \rightarrow 'O_2^-$$

Photodegradation of isoproturon

ISP + OH' + O_2 \rightarrow degradation product (CO₂ and H₂O)

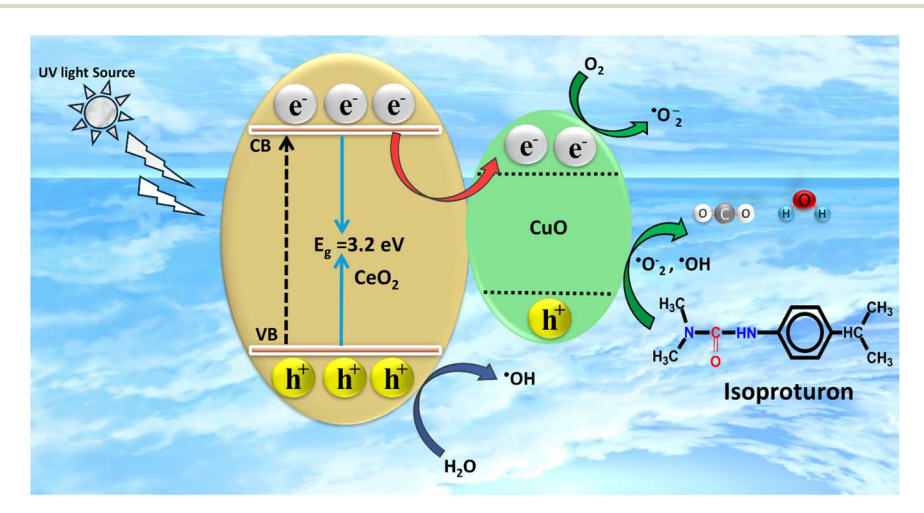


Fig. 6 Schematic of the degradation pathway for IPU using CuO/CeO₂ nanocomposites under UV light irradiation.

Fig. 7 IPU degradation intermediates detected using HRMS analysis.

4.1 Identification of IPU degradation intermediates

The UV-vis absorption spectra in Fig. 5b show that IPU in an aqueous solution is completely degraded under UV light irradiation with the CuO/CeO₂ catalyst. However, the exact pathway to degradation is not clear. Therefore, based on the relevant literature, the pathway and the intermediate products involved in the photodegradation of IPU during the process have been identified using HRMS. Here, we have discussed three possible degradation pathways based on the results of HRMS with the m/ z values of corresponding intermediates, which are consistent with the previous literature. The degradation of the IPU molecule, (3-(4-isopropylphenyl)-1,1-dimethylurea, m/z = 207), into the intermediates at m/z values of 192, 178, 135 and 120, is illustrated in the degradation pathway-I (Fig. 7). The observed intermediate P1 (m/z = 192) 1-(4-isopropylphenyl)-3-methylurea⁹¹ corresponds to the cleavage of a methyl group from the dimethylurea moiety in the IPU molecule, followed by the fragmentation of the other methyl group, resulting in the intermediate P2 (m/z = 178) 1-(4-isopropylphenyl)urea. 92 The subsequent fragmentation gives the intermediate P3 (m/z = 135) 4-isopropylaniline.93 Afterward, the removal of the methyl group yields the intermediate P4 (m/z = 120) 4-ethylaniline.⁹⁴ Possible alternative degradation pathways were identified, with m/z values, revealing various intermediate compounds (Fig. S12 and S13†). The HRMS results and UV spectra suggest that IPU is degraded into CO2 and H2O.95

5 Photostability and recyclability

The stability and reusability of CuO/CeO_2 nanocomposites were assessed by photocatalytic degradation recycling experiments under UV-light irradiation. After conducting each run, the CuO/CeO_2 nanocomposite was washed with ethanol twice and dried at 80 °C for 3 h. Fig. 5e shows the photocatalytic degradation efficiency of IPU after 3 cycles, with a slight decrease from 95% to 85%. Therefore, it can be suggested that the CuO/CeO_2

nanocomposites exhibit good stability under UV-light irradiation.

6 Conclusions

In this work, we prepared a CuO/CeO₂ catalyst with enhanced defects on the surface of CeO2 and evaluated its catalytic performance for the degradation of isoproturon under UV light irradiation. There was a marked change in catalytic performance with an increase in defects caused by the interaction between CuO and CeO2. Aiming to characterize the defects, oxygen vacancies on the surface of CeO₂ were quantitatively estimated. By evaluating the catalytic performance of the prepared catalyst CuO/CeO₂, the role of oxygen vacancies in the catalysis was proved. The suppression of the rate of the electron-hole recombination process, consequently increasing the lifetime of photogenerated charge carriers, which is a favorable factor for the enhancement of photocatalytic performance, was established by the photoluminescence studies. The incorporation of CuO into CeO₂ led to several significant modifications: (i) a slight narrowing of the band gap from 3.3 eV (pristine CeO₂) to 3.2 eV in CuO/CeO₂, (ii) an increase in the oxygen vacancies within the CeO2 lattice, which is expressed by the higher concentration of Ce3+, (iii) an enhanced transfer of photogenerated electrons from the conduction band (CB) to oxygen molecules and (iv) restrained recombination of photogenerated e⁻ and h⁺ pairs. The active species responsible for the degradation of IPU were identified to be 'OH and 'O₂⁻ radicals. The HR-MS analysis reveals the degradation intermediates of IPU and its possible degradation pathways. By integrating insights from the catalyst characterization and photocatalysis experiments, a potential reaction mechanism for the degradation of IPU in water was suggested. Additionally, recycling studies confirmed the stability of the catalyst with a minimal reduction in activity even after three consecutive cycles. These insights into the defects in CeO2 and their role in photocatalysis could

provide guidance for designing high-performance CeO₂-based catalysts.

Data availability

Paper

The data supporting this article have been included as part of the ESI.†

Author contributions

A. K. Dhanka: methodology, investigation, writing draft, formal analysis. Balaram Pani: data curation, formal analysis and editing. Nityananda Agasti: supervision, investigation, data curation, formal analysis, writing, review & editing, and editing the final manuscript.

Conflicts of interest

The authors declare no competing financial interest.

Acknowledgements

Ajit Kumar Dhanka thanks the Council of Scientific & Industrial Research (CSIR) and University Grants Commission (UGC) for the Junior Research Fellowship (JRF)-16-6(119119 Dec. 2018/19). The authors would also like to acknowledge Deen Dayal Upadhyaya College University of Delhi, University Science Instrumentation Centre (USIC), University of Delhi, Special Center for Nanoscience, Jawaharlal Nehru University (JNU), New Delhi, Central Instrumentation Facility (CRF), Jamia Millia Islamia, New Delhi and the Department of Materials Science and Engineering (DMSE), Indian Institute of Technology (IIT) Delhi, New Delhi, India for the characterization facilities. The Sophisticated Analytical Instrumentation Facility (SAIF) at the All India Institute of Medical Sciences (AIIMS), New Delhi, is acknowledged for the HRTEM measurements.

References

- 1 K. Khan, F. Khitab, J. Shah and M. R. Jan, Ultrasound assisted photocatalytic degradation of isoproturon and triasulfuron herbicides using visible light driven impregnated zinc oxide catalysts, *Sustainable Environ. Res.*, 2023, 33(1), 24, DOI: 10.1186/s42834-023-00184-9.
- 2 M. Tudi, H. Daniel Ruan, L. Wang, J. Lyu, R. Sadler, D. Connell, C. Chu and D. T. Phung, Agriculture development, pesticide application and its impact on the environment, *Int. J. Environ. Res. Public Health*, 2021, 18(3), 1112, DOI: 10.3390/ijerph180311.
- 3 A. Sharma, V. Kumar, B. Shahzad, M. Tanveer, G. P. Sidhu, N. Handa, S. K. Kohli, P. Yadav, A. S. Bali, R. D. Parihar and O. I. Dar, Worldwide pesticide usage and its impacts on ecosystem, *SN Appl. Sci.*, 2019, 1, 1–6, DOI: 10.1007/s42452-019-1485-1.
- 4 M. J. García-Galán, L. S. Monllor-Alcaraz, C. Postigo, E. Uggetti, M. L. de Alda, R. Díez-Montero and J. García, Microalgae-based bioremediation of water contaminated by

- pesticides in peri-urban agricultural areas, *Environ. Pollut.*, 2020, 265, 114579, DOI: 10.1016/j.envpol.2020.114579.
- 5 Y. Wen, M. Feng, P. Zhang, H. C. Zhou, V. K. Sharma and X. Ma, Metal organic frameworks (MOFs) as photocatalysts for the degradation of agricultural pollutants in water, *ACS ES&T Eng.*, 2021, 1(5), 804–826, DOI: 10.1021/acsestengg.1c00051.
- 6 M. Rossides, C. E. Kampitsi, M. Talbäck, H. Mogensen, P. Wiebert, G. Tettamanti and M. Feychting, Occupational exposure to pesticides in mothers and fathers and risk of cancer in the offspring: A register-based case-control study from Sweden (1960–2015), *Environ. Res.*, 2022, 214, 113820, DOI: 10.1016/j.envres.2022.113820.
- 7 A. J. De Roos, L. H. Schinasi, L. Miligi, J. R. Cerhan, P. Bhatti, A. 't Mannetje, D. Baris, Y. Benavente, G. Benke, J. Clavel and D. Casabonne, Occupational insecticide exposure and risk of n on-Hodgkin lymphoma: A pooled c ase-control study from the InterLymph Consortium, *Int. J. Cancer*, 2021, 149(10), 1768–1786, DOI: 10.1002/ijc.33740.
- 8 A. Sikder, A. K. Pearce, S. J. Parkinson, R. Napier and R. K. O'Reilly, Recent trends in advanced polymer materials in agriculture related applications, ACS Appl. Polym. Mater., 2021, 3(3), 1203–1217, DOI: 10.1021/ acsapm.0c00982.
- 9 T. T. Hoang, C. Qi, K. C. Paul, M. Lee, J. D. White, M. Richards, S. S. Auerbach, S. Long, S. Shrestha, T. Wang and L. E. Beane Freeman, Epigenome-wide DNA methylation and pesticide use in the agricultural lung health study, *Environ. Health Perspect.*, 2021, 129(9), 097008, DOI: 10.1289/EHP8928.
- 10 M. E. Leon, L. H. Schinasi, P. Lebailly, L. E. Beane Freeman, K. C. Nordby, G. Ferro, A. Monnereau, M. Brouwer, S. Tual, I. Baldi and K. Kjaerheim, Pesticide use and risk of non-Hodgkin lymphoid malignancies in agricultural cohorts from France, Norway and the USA: a pooled analysis from the AGRICOH consortium, *Int. J. Epidemiol.*, 2019, 48(5), 1519–1535, DOI: 10.1093/ije/dyz017.
- 11 X. Liu, S. Xiang, T. Zong, G. Ma, L. Wu, K. Liu, X. Zhou and L. Bai, Herbicide resistance in China: a quantitative review, *Weed Sci.*, 2019, 67(6), 605–612, DOI: 10.1017/wsc.2019.46.
- 12 N. I. Elarabi, A. A. Abdelhadi, A. A. Nassrallah, M. S. Mohamed and H. A. Abdelhaleem, Biodegradation of isoproturon by Escherichia coli expressing a Pseudomonas putida catechol 1, 2-dioxygenase gene, *AMB Express*, 2023, 13(1), 101, DOI: 10.1186/s13568-023-01609-9.
- 13 R. Leoci and M. Ruberti, Isoproturon: A Controversial Herbicide Hard to Confine in a Global Market, *J. Sustain. Dev.*, 2024, 13(6), 1–43, DOI: 10.5539/jsd.v13n6p43.
- 14 M. Mansour, E. A. Feicht, A. Behechti and I. Scheunert, Experimental approaches to studying the photostability of selected pesticides in water and soil, *Chemosphere*, 1997, 35(1–2), 39–50, DOI: 10.1016/j.jksus.2020.08.020.
- 15 S. Thomas, A. Alatrache, M. N. Pons and O. Zahraa, Degradation of the herbicide isoproturon by a photocatalytic process, *C. R. Chim.*, 2014, 17(7–8), 824–831, DOI: 10.1016/j.crci.2014.04.002.

- 16 L. Arnaud, G. Taillandier, M. Kaouadji, P. Ravanel and M. Tissut, Photosynthesis inhibition by phenylureas: A QSAR approach, *Ecotoxicol. Environ. Saf.*, 1994, 28(2), 121– 133, DOI: 10.1006/eesa.1994.1040.
- 17 R. de Oliveira, W. da Silva Martini and A. C. Sant'Ana, Combined effect involving semiconductors and plasmonic nanoparticles in photocatalytic degradation of pesticides, *Environ. Nanotechnol., Monit. Manage.*, 2022, 17, 100657, DOI: 10.1016/j.enmm.2022.100657.
- 18 T. T. Duong, C. Y. Guan, G. B. Hong and C. T. Chang, Specifically designed 10-Fe, *Sustainable Environ. Res.*, 2023, 33, 15, DOI: 10.1186/s42834-023-00173-y.
- 19 R. Leoci and M. Ruberti, Isoproturon: a controversial herbicide hard to confine in a global market, *J. Sustain. Dev.*, 2020, **12**, 43–54, DOI: **10**.5539/jsd.v13n6p43.
- 20 K. M. Moore, S. R. Jones and C. James, Multi-residue analytical method for uron and carbamate pesticides in water using solid-phase extraction and liquid chromatography-mass spectrometry, *Water Res.*, 1995, 29(5), 1225–1230, DOI: 10.1016/0043-1354(94)00321-W.
- 21 J. Durak, T. Rokoszak, A. Skiba, P. Furman and K. Styszko, Environmental risk assessment of priority biocidal substances on Polish surface water sample, *Environ. Sci. Pollut. Res.*, 2021, 28, 1254–1266, DOI: 10.1007/s11356-020-11581-7.
- 22 S. Belz, C. Cella, O. Geiss, D. Gilliland, R. La Spina, D. M\u00e9hn and B. Sokull-Kluettgen, Analytical Methods to Measure Microplastics in Drinking Water, Publications Office of the European Union, Luxembourg, 2024, DOI: 10.2760/109944.
- 23 European Commission, Commission implementing Regulation (EU) 2016/872 of 1 June 2016 concerning the non-renewal of approval of the active substance isoproturon, in accordance with Regulation (EC) No 1107/2009 of the European Parliament and of the Council concerning the placing of plant protection products on the market and amending Commission Implementing Regulation (EU) No 540/2011, 2016, retrieved from https://data.europa.eu/eli/reg_impl/2016/872/oj.
- 24 Y. C. Lu, S. Zhang, S. S. Miao, C. Jiang, M. T. Huang, Y. Liu and H. Yang, Enhanced degradation of herbicide isoproturon in wheat rhizosphere by salicylic acid, *J. Agric. Food Chem.*, 2015, 63(1), 92–103, DOI: 10.1021/jf505117j.
- 25 Conclusion on the peer review of the pesticide risk assessment of the active substance ferric phosphate, *EFSA J.*, 2015, **13**(1), 3973, DOI: **10.2903/j.efsa.2015.3973**.
- 26 L. K. Chauhan, M. Kumar, B. N. Paul, S. K. Goel and S. K. Gupta, Cytogenetic effects of commercial formulations of deltamethrin and/or isoproturon on human peripheral lymphocytes and mouse bone marrow cells, *Environ. Mol. Mutagen.*, 2007, 48(8), 636–643, DOI: 10.1002/em.20330.
- 27 H. A. Pereira, K. da Boit Martinello, Y. Vieira, J. C. Diel, M. S. Netto, G. D. Reske, E. Lorenzett, L. F. Silva, T. A. Burgo and G. L. Dotto, Adsorptive behavior of multiwalled carbon nanotubes immobilized magnetic nanoparticles for removing selected pesticides from aqueous matrices, *Chemosphere*, 2023, 325, 138384, DOI: 10.1016/j.chemosphere.2023.138384.

- 28 A. Kar, S. Deole, B. G. Gadratagi, N. Patil, G. Guru-Pirasanna-Pandi, B. Mahapatra and T. Adak, Facile synthesis of novel magnesium oxide nanoparticles for pesticide sorption from water, *Environ. Sci. Pollut. Res.*, 2023, **30**(45), 101467–101482, DOI: 10.1007/s11356-023-29562-x.
- 29 M. Samari, R. Heydari and F. Gholami, Nanofiltration membrane functionalized with CuxP nanoparticles: a promising approach for enhanced pesticide removal and long-term stability, *J. Cleaner Prod.*, 2024, 445, 141352, DOI: 10.1016/j.jclepro.2024.141352.
- 30 A. K. Pereira, L. F. Silva, G. A. Barbosa, T. G. Miranda, R. R. Sousa, R. A. Sarmento, N. L. Souza, D. H. Pereira and G. S. Cavallini, The socio-environmental and human health problems related to the use of pesticides and the use of advanced oxidative processes for their degradation: Brazil, *Water*, 2023, 15(8), 1608, DOI: 10.3390/w15081608.
- 31 N. Ates, N. Uzal, U. Yetis and F. B. Dilek, Removal of pesticides from secondary treated urban wastewater by reverse osmosis, *Environ. Sci. Pollut. Res.*, 2023, 30(4), 8732–8745, DOI: 10.1007/s11356-022-20077-5.
- 32 L. Yang, F. Xue and D. He, Removal of six pesticide residues from vegetables by the coupled ultrasonic-ozonation process, *Food Control*, 2024, **155**, 110109, DOI: **10.1016**/j.foodcont.2023.110109.
- 33 L. Yang, F. Xue and D. He, Removal of six pesticide residues from vegetables by the coupled ultrasonic-ozonation process, *Food Control*, 2024, **155**, 110109, DOI: **10.1016**/j.watres.2022.119447.
- 34 A. S. Raj, G. Anup, R. Sivalingam and P. Chandran, Biodegradation of chlorpyrifos by charcoal–alginate immobilized bacterial consortium isolated from pesticide-polluted Kuzhikandam Creek, Kerala, India, *Biorem. J.*, 2024, 28(4), 491–511, DOI: 10.1080/10889868.2024.2312463.
- 35 T. P. Giang, N. S. Nguyen, H. T. Dao, Q. K. Dang and T. Q. Tran, Boosting degradation of synthetic dye and pesticide residues in Water using NCDs/FeNH₂BDC photocatalysts, *Top. Catal.*, 2024, **67**(9), 761–772, DOI: **10.1007/s11244-023-01900-w**.
- 36 H. Targhan, A. Rezaei, A. Aliabadi, H. Zheng, H. Cheng and T. M. Aminabhavi, Adsorptive and photocatalytic degradation of imidacloprid pesticide from wastewater via the fabrication of ZIF-CdS/Tpy quantum dots, *Chem. Eng. J.*, 2024, **482**, 148983, DOI: **10.1016/j.cej.2024.148983**.
- 37 B. F. Abramović, M. M. Uzelac, S. J. Armaković, U. Gašić, D. D. Četojević-Simin and S. Armaković, Experimental and computational study of hydrolysis and photolysis of antibiotic ceftriaxone: Degradation kinetics, pathways, and toxicity, *Sci. Total Environ.*, 2021, 768, 144991, DOI: 10.1016/j.scitotenv.2021.144991.
- 38 B. F. Abramović, M. M. Uzelac, S. J. Armaković, U. Gašić, D. D. Četojević-Simin and S. Armaković, Experimental and computational study of hydrolysis and photolysis of antibiotic ceftriaxone: Degradation kinetics, pathways, and toxicity, *Sci. Total Environ.*, 2021, 768, 144991, DOI: 10.1016/j.cej.2023.145221.
- 39 J. Chen, T. Tang, W. Feng, X. Liu, Z. Yin, X. Zhang, J. Chen and S. Cao, Large-scale synthesis of p-n heterojunction

Bi₂O₃/TiO₂ nanostructures as photocatalysts for removal of antibiotics under visible light, *ACS Appl. Nano Mater.*, 2021, 5(1), 1296–1307, DOI: 10.1021/acsanm.1c03851.

- 40 S. Kumar, R. Sharma, A. Gupta, A. Tyagi, P. Singh, A. Kumar and V. Kumar, Recent insights into SnO₂-based engineered nanoparticles for sustainable H 2 generation and remediation of pesticides, *New J. Chem.*, 2022, **46**(9), 4014–4048, DOI: **10.1039/D1NJ05808H**.
- 41 K. Hu, Q. Xie, H. Wang, B. Zhang, Y. Huang, S. Song, H. Zhang, Y. Ding, H. Huang and C. Wu, Synergistic catalysis of Cu-CeO₂@CA composite film in a circulating DBD plasma system and its effect on ciprofloxacin degradation, *Chem. Eng. J.*, 2023, 455, 140895, DOI: 10.1016/j.cej.2022.140895.
- 42 K. Hashimoto, H. Irie and A. Fujishima, TiO₂ photocatalysis: a historical overview and future prospects, *Jpn. J. Appl. Phys.*, 2005, 44(12R), 8269, DOI: 10.1143/JJAP.44.8269.
- 43 D. Zhang, Y. Qian, L. Shi, H. Mai, R. Gao, J. Zhang, W. Yu and W. Cao, Cu-doped CeO₂ spheres: synthesis, characterization, and catalytic activity, *Catal. Commun.*, 2012, 26, 164–168, DOI: 10.1016/j.catcom.2012.05.001.
- 44 A. Taratayko, E. Kolobova and G. Mamontov, Graphene oxide decorated with Ag and CeO₂ nanoparticles as a catalyst for room-temperature 4-nitrophenol reduction, *Catalysts*, 2022, 12(11), 1393, DOI: 10.3390/catal12111393.
- 45 A. Rianjanu, K. D. Marpaung, C. Siburian, S. A. Muhtar, N. I. Khamidy, J. Widakdo, N. Yulianto, R. Aflaha, K. Triyana and T. Taher, Enhancement of photocatalytic activity of CeO₂ nanorods through lanthanum doping (La– CeO₂) for the degradation of Congo red dyes, *Results Eng.*, 2024, 23, 102748, DOI: 10.1016/j.rineng.2024.102748.
- 46 K. Zhong, P. Sun and H. Xu, Advances in defect engineering of metal oxides for photocatalytic CO₂ reduction, *Small*, 2024, 2310677, DOI: 10.1002/smll.202310677.
- 47 A. Haghighatzadeh, Enhanced third-order optical susceptibility in Ag-doped CeO₂ nanostructures under pulsed Nd-YVO₄ laser, *Opt Laser. Technol.*, 2020, 126, 106114, DOI: 10.1016/j.optlastec.2020.106114.
- 48 A. K. Dhanka, E. C. Kohlrausch, R. Samantray, V. Kumar, B. Pani and N. Agasti, Harnessing defects in Ag/CeO₂ for enhanced photocatalytic degradation of antibiotic in water: Structural characteristics, in-depth insights on mechanism, degradation pathway, *Chem. Eng. J. Adv.*, 2025, 21, 100706, DOI: 10.1016/j.ceja.2025.100706.
- 49 K. Dulta, G. Koşarsoy Ağçeli, P. Chauhan, R. Jasrotia, P. K. Chauhan and J. O. Ighalo, Multifunctional CuO nanoparticles with enhanced photocatalytic dye degradation and antibacterial activity, *Sustainable Environ. Res.*, 2022, 32, 1–5, DOI: 10.1186/s42834-021-00111-w.
- 50 I. Nurhasanah, W. Safitri, Z. Arifin, A. Subagio and T. Windarti, Antioxidant activity and dose enhancement factor of CeO₂ nanoparticles synthesized by precipitation method, *IOP Conf. Ser.:Mater. Sci. Eng.*, 2018, 432, 012031, DOI: 10.1088/1757-899X/432/1/012031.
- 51 R. ChithraDevi, S. Surendhiran, A. Balamurugan, P. Bhoopathy, K. Kandasamy and Y. A. Khadar, Evaluation of antibacterial activity and anticorrosive inhibition

- behaviour of copper doped cerium oxide nanoparticles (Cu-CeO₂ NPs), *AIP Conf. Proc.*, 2022, **2385**(1), DOI: **10.1063/5.0070804**.
- 52 K. W. Aga, M. T. Efa and T. T. Beyene, Effects of sulfur doping and temperature on the energy bandgap of ZnO nanoparticles and their antibacterial activities, *ACS Omega*, 2022, 7(12), 10796–10803, DOI: 10.1021/acsomega.2c00647.
- 53 S. Selvaraj, M. K. Mohan, M. Navaneethan, S. Ponnusamy and C. Muthamizhchelvan, Synthesis and photocatalytic activity of Gd doped ZnO nanoparticles for enhanced degradation of methylene blue under visible light, *Mater. Sci. Semicond. Process.*, 2019, 103, 104622, DOI: 10.1016/ j.mssp.2019.104622.
- 54 F. Su, P. Li, J. Huang, M. Gu, Z. Liu and Y. Xu, Photocatalytic degradation of organic dye and tetracycline by ternary Ag₂O/AgBr–CeO₂ photocatalyst under visible-light irradiation, *Sci. Rep.*, 2021, 11(1), 85, DOI: 10.1038/s41598-020-76997-0.
- 55 K. N. Pandiyaraj, D. Vasu, M. C. Ramkumar, R. R. Deshmukh and R. Ghobeira, Improved degradation of textile effluents via the synergetic effects of Cu-CeO₂ catalysis and non-thermal atmospheric pressure plasma treatment, *Sep. Purif. Technol.*, 2021, 258, 118037, DOI: 10.1016/j.seppur.2020.118037.
- 56 A. Jafari, S. A. Terohid, A. Kokabi and A. Moradiani, Electrical, structural, and photocatalytic properties of copper oxide nanowire, *J. Chem. Res.*, 2020, 44(7–8), 471–474, DOI: 10.1177/1747519819899068.
- 57 G. Manibalan, G. Murugadoss, R. Thangamuthu, P. Ragupathy, R. M. Kumar and R. Jayavel, Enhanced electrochemical supercapacitor and excellent amperometric sensor performance of heterostructure CeO₂-CuO nanocomposites via chemical route, *Appl. Surf. Sci.*, 2018, 456, 104–113, DOI: 10.1016/j.apsusc.2018.06.071.
- 58 Y. Li, Y. Cai, X. Xing, N. Chen, D. Deng and Y. Wang, Catalytic activity for CO oxidation of Cu–CeO₂ composite nanoparticles synthesized by a hydrothermal method, *Anal. Methods*, 2015, 7(7), 3238–3245, DOI: 10.1039/C5AY00261C.
- 59 S. Mustapha, M. M. Ndamitso, A. S. Abdulkareem, J. O. Tijani, D. T. Shuaib, A. K. Mohammed and A. Sumaila, Comparative study of crystallite size using Williamson-Hall and Debye-Scherrer plots for ZnO nanoparticles, *Adv. Nat. Sci.:Nanosci. Nanotechnol.*, 2019, 10(4), 045013, DOI: 10.1088/2043-6254/ab52f7.
- 60 M. M. Khan, S. A. Ansari, D. Pradhan, D. H. Han, J. Lee and M. H. Cho, Defect-induced band gap narrowed CeO₂ nanostructures for visible light activities, *Ind. Eng. Chem. Res.*, 2014, 53(23), 9754–9763, DOI: 10.1021/ie500986n.
- 61 N. Agasti, M. A. Astle, G. A. Rance, J. Alves Fernandes, J. Dupont and A. N. Khlobystov, Cerium oxide nanoparticles inside carbon nanoreactors for selective allylic oxidation of cyclohexene, *Nano Lett.*, 2020, 20(2), 1161–1171, DOI: 10.1021/acs.nanolett.9b04579.
- 62 J. F. Xu, W. Ji, Z. X. Shen, W. S. Li, S. H. Tang, X. R. Ye, D. Z. Jia and X. Q. Xin, Raman spectra of CuO nanocrystals, *J. Raman Spectrosc.*, 1999, 30(5), 413–415, DOI: 10.1002/(SICI)1097-4555(199905)30:5<413::AID-JRS387>3.0.CO;2-N.

- 63 C. Schilling, A. Hofmann, C. Hess and M. V. Ganduglia-Pirovano, Raman spectra of polycrystalline CeO₂: a density functional theory study, *J. Phys. Chem. C*, 2017, **121**(38), 20834–20849, DOI: **10.1021/acs.jpcc.7b06643**.
- 64 E. Swatsitang, S. Phokha, S. Hunpratub and S. Maensiri, Modification of Ce valence states by Sm/Sr co-doping of CeO₂ nanoparticles for improved magneto-electrochemical properties, *Mater. Des.*, 2016, **108**, 27–33, DOI: **10.1016**/j.matdes.2016.06.092.
- 65 L. Ilieva, P. Petrova, G. Pantaleo, R. Zanella, L. F. Liotta, V. Georgiev, S. Boghosian, Z. Kaszkur, J. W. Sobczak, W. Lisowski and A. M. Venezia, Gold catalysts supported on Y-modified ceria for CO-free hydrogen production via PROX, *Appl. Catal., B*, 2016, 188, 154–168, DOI: 10.1016/j.apcatb.2016.02.004.
- 66 Z. Wu, M. Li, J. Howe, I. I. I. H. M. Meyer and S. H. Overbury, Probing defect sites on CeO₂ nanocrystals with well-defined surface planes by Raman spectroscopy and O₂ adsorption, *Langmuir*, 2010, 26(21), 16595–16606, DOI: 10.1021/ la101723w.
- 67 J. M. López, A. L. Gilbank, T. García, B. Solsona, S. Agouram and L. Torrente-Murciano, The prevalence of surface oxygen vacancies over the mobility of bulk oxygen in nanostructured ceria for the total toluene oxidation, *Appl. Catal., B*, 2015, 174, 403–412, DOI: 10.1016/j.apcatb.2015.03.017.
- 68 P. Trogadas, J. Parrondo and V. Ramani, CeO₂ surface oxygen vacancy concentration governs in situ free radical scavenging efficacy in polymer electrolytes, ACS Appl. Mater. Interfaces, 2012, 4(10), 5098–5102, DOI: 10.1021/am3016069.
- 69 W. H. Weber, K. C. Hass and J. R. McBride, Raman study of CeO₂: Second-order scattering, lattice dynamics, and particle-size effects, *Phys. Rev. B:Condens. Matter Mater. Phys.*, 1993, **48**(1), 178, DOI: **10.1103/PhysRevB.48.178**.
- 70 K. Kumari, R. N. Aljawfi, Y. S. Katharria, S. Dwivedi, K. H. Chae, R. Kumar, A. Alshoaibi, P. A. Alvi, S. Dalela and S. Kumar, Study the contribution of surface defects on the structural, electronic structural, magnetic, and photocatalyst properties of Fe: CeO₂ nanoparticles, *J. Electron Spectrosc. Relat. Phenom.*, 2019, 235, 29–39, DOI: 10.1016/j.elspec.2019.06.004.
- 71 W. Cai, Y. Shi, Y. Zhao, M. Chen, Q. Zhong and Y. Bu, The solvent-driven formation of multi-morphological Ag-CeO₂ plasmonic photocatalysts with enhanced visible-light photocatalytic reduction of CO₂, RSC Adv., 2018, 8(71), 40731–40739, DOI: 10.1039/C8RA08938H.
- 72 A. L. Cámara, V. C. Corberán, A. Martínez-Arias, L. Barrio, R. Si, J. C. Hanson and J. A. Rodriguez, Novel manganese-promoted inverse CeO₂/CuO catalyst: In situ characterization and activity for the water-gas shift reaction, *Catal. Today*, 2020, 339, 24–31, DOI: 10.1016/j.cattod.2019.01.014.
- 73 W. Li, S. Xie, M. Li, X. Ouyang, G. Cui, X. Lu and Y. Tong, CdS/CeO_x heterostructured nanowires for photocatalytic hydrogen production, *J. Mater. Chem. A*, 2013, **1**(13), 4190–4193, DOI: **10.1039/C3TA10394C**.

- 74 X. J. Wen, C. G. Niu, L. Zhang, C. Liang and G. M. Zeng, A novel Ag₂O/CeO₂ heterojunction photocatalysts for photocatalytic degradation of enrofloxacin: possible degradation pathways, mineralization activity and an in depth mechanism insight, *Appl. Catal., B,* 2018, **221**, 701–714, DOI: **10.1016/j.apcatb.2017.09.060**.
- 75 P. Muthukumar, M. Pannipara, A. G. Al-Sehemi and S. P. Anthony, Highly enhanced bifunctional electrocatalytic activity of mixed copper–copper oxides on nickel foam via composition control, *New J. Chem.*, 2020, 44(28), 11993–12001, DOI: 10.1039/D0NJ02311F.
- 76 Z. Jin, C. Liu, K. Qi and X. Cui, Photo-reduced Cu/CuO nanoclusters on TiO₂ nanotube arrays as highly efficient and reusable catalyst, *Sci. Rep.*, 2017, 7(1), 39695, DOI: 10.1038/srep39695.
- 77 P. Dutta, S. Pal, M. S. Seehra, Y. Shi, E. M. Eyring and R. D. Ernst, Concentration of Ce³⁺ and oxygen vacancies in cerium oxide nanoparticles, *Chem. Mater.*, 2006, **18**(21), 5144–5146, DOI: **10.1021/cm061580n**.
- 78 D. R. Mullins, S. H. Overbury and D. R. Huntley, Electron spectroscopy of single crystal and polycrystalline cerium oxide surfaces, *Surf. Sci.*, 1998, **409**(2), 307–319, DOI: **10.1016/S0039-6028(98)00257-X**.
- 79 J. Chen, S. Shen, P. Wu and L. Guo, Nitrogen-doped CeO x nanoparticles modified graphitic carbon nitride for enhanced photocatalytic hydrogen production, *Green Chem.*, 2015, 17(1), 509–517, DOI: 10.1039/C4GC01683A.
- 80 F. Tang, C. Mei, P. Chuang, T. Song, H. Su, Y. Wu, Y. Qiao, J. C. Huang and Y. F. Liao, Valence state and magnetism of Mn-doped PbPdO₂ nanograin film synthesized by sol-gel spin-coating method, *Thin Solid Films*, 2017, 623, 14–18, DOI: 10.1016/j.tsf.2016.12.043.
- 81 J. Li, Z. Liu, D. A. Cullen, W. Hu, J. Huang, L. Yao, Z. Peng, P. Liao and R. Wang, Distribution and valence state of Ru species on CeO₂ supports: support shape effect and its influence on CO oxidation, ACS Catal., 2019, 9(12), 11088– 11103, DOI: 10.1021/acscatal.9b03113.
- 82 P. K. Yadav, K. Patrikar, A. Mondal and S. Sharma, Ni/Co in and on CeO₂: a comparative study on the dry reforming reaction, *Sustainable Energy Fuels*, 2023, 7(16), 3853–3870, DOI: 10.1039/D3SE00649B.
- 83 Z. Ren, F. Peng, J. Li, X. Liang and B. Chen, Morphology-dependent properties of Cu/CeO₂ catalysts for the watergas shift reaction, *Catalysts*, 2017, 7(2), 48, DOI: 10.3390/catal7020048.
- 84 M. I. Al-Zaben and A. A. Alghamdi, Gamma ray irradiation assisted decomposition for isoproturon pesticide in aqueous solutions: A detailed study, *J. King Saud Univ., Sci.*, 2020, 32(7), 3097–3102, DOI: 10.1016/j.jksus.2020.08.020.
- 85 C. Tixier, L. Meunier, F. Bonnemoy and P. Boule, Phototransformation of three herbicides: chlorbufam, isoproturon, and chlorotoluron. Influence of irradiation on toxicity, *Int. J. Photoenergy*, 2000, 2(1), 1–8, DOI: 10.1155/S1110662X00000015.
- 86 R. A. Amoresi, R. C. Oliveira, N. L. Marana, P. B. De Almeida,
 P. S. Prata, M. A. Zaghete, E. Longo, J. R. Sambrano and
 A. Z. Simoes, CeO₂ nanoparticle morphologies and their

corresponding crystalline planes for the photocatalytic degradation of organic pollutants, *ACS Appl. Nano Mater.*, 2019, **2**(10), 6513–6526, DOI: **10.1021/acsanm.9b01452**.

- 87 T. M. Berhane, J. Levy, M. P. Krekeler and N. D. Danielson, Kinetic sorption of contaminants of emerging concern by a palygorskite-montmorillonite filter medium, *Chemosphere*, 2017, 176, 231–242, DOI: 10.1016/j.chemosphere.2017.02.068.
- 88 J. López-Luna, L. E. Ramírez-Montes, S. Martinez-Vargas, A. I. Martínez, O. F. Mijangos-Ricardez, M. D. González-Chávez, R. Carrillo-González, F. A. Solís-Domínguez, M. D. Cuevas-Díaz and V. Vázquez-Hipólito, Linear and nonlinear kinetic and isotherm adsorption models for arsenic removal by manganese ferrite nanoparticles, SN Appl. Sci., 2019, 1, 1–9, DOI: 10.1007/s42452-019-0977-3.
- 89 Q. Leng, D. Yang, Q. Yang, C. Hu, Y. Kang, M. Wang and M. Hashim, Building novel Ag/CeO₂ heterostructure for enhancing photocatalytic activity, *Mater. Res. Bull.*, 2015, 65, 266–272, DOI: 10.1016/j.materresbull.2015.02.008.
- 90 C. Yang, J. Yang, X. Duan, G. Hu, Q. Liu, S. Ren, J. Li and M. Kong, Roles of photo-generated holes and oxygen vacancies in enhancing photocatalytic performance over CeO₂ prepared by molten salt method, Adv. Powder

- *Technol.*, 2020, 31(9), 4072–4081, DOI: 10.1016/j.apt.2020.08.017.
- 91 Y. C. Lu, S. Zhang and H. Yang, Acceleration of the herbicide isoproturon degradation in wheat by glycosyltransferases and salicylic acid, *J. Hazard. Mater.*, 2015, **283**, 806–814, DOI: **10.1016/j.jhazmat.2014.10.034**.
- 92 Y. C. Lu, S. Zhang and H. Yang, Acceleration of the herbicide isoproturon degradation in wheat by glycosyltransferases and salicylic acid, *J. Hazard. Mater.*, 2015, **283**, 806–814, DOI: **10.1016/j.jhazmat.2014.10.034**.
- 93 P. P. Choudhury, Leaf cuticle-assisted phototransformation of isoproturon, *Acta Physiol. Plant.*, 2017, 39(8), 188, DOI: 10.1007/s11738-017-2471-0.
- 94 Y. C. Lu, S. Zhang and H. Yang, Acceleration of the herbicide isoproturon degradation in wheat by glycosyltransferases and salicylic acid, *J. Hazard. Mater.*, 2015, **283**, 806–814, DOI: **10.1016/j.jhazmat.2014.10.034**.
- 95 K. Khan, F. Khitab, J. Shah and M. R. Jan, Ultrasound assisted photocatalytic degradation of isoproturon and triasulfuron herbicides using visible light driven impregnated zinc oxide catalysts, *Sustainable Environ. Res.*, 2023, 33(1), 24, DOI: 10.1186/s42834-023-00184-9.